Anisotropic failure and size effects in periodic honeycomb materials: A gradient-elasticity approach

Julien Réthoré, Thi Bach Tuyet Dang, Christine Kaltenbrunner

▶ **To cite this version:**

Julien Réthoré, Thi Bach Tuyet Dang, Christine Kaltenbrunner. Anisotropic failure and size effects in periodic honeycomb materials: A gradient-elasticity approach. Journal of the Mechanics and Physics of Solids, 2017, 99, pp.35-49. 10.1016/j.jmps.2016.10.013 . hal-03770073

HAL Id: hal-03770073
https://hal.science/hal-03770073

Submitted on 6 Sep 2022

HAL is a multi-disciplinary open access archive for the deposit and dissemination of scientific research documents, whether they are published or not. The documents may come from teaching and research institutions in France or abroad, or from public or private research centers.

L'archive ouverte pluridisciplinaire **HAL**, est destinée au dépôt et à la diffusion de documents scientifiques de niveau recherche, publiés ou non, émanant des établissements d'enseignement et de recherche français ou étrangers, des laboratoires publics ou privés.

Anisotropic failure and size effects in periodic honeycomb materials: a gradient-elasticity approach

Julien Réthoré[1], Thi Bach Tuyet Dang, Christine Kaltenbrunner

LaMCoS, Université de Lyon / INSA Lyon / CNRS UMR 5259
Bat. Jacquard, 27 Avenue Jean Capelle, F-69621 Villeurbanne, Cedex, France

Abstract

This paper proposes a fracture mechanics model for the analysis of crack propagation in periodic honeycomb materials. The model is based on gradient-elasticity what enables to account for the effect of the material structure at the macroscopic scale. For simulating the propagation of cracks along an arbitrary path, the numerical implementation is elaborated based on an extended finite element method with the required level of continuity. The two main features captured by the model are directionality and size effect. The numerical predictions are consistent with experimental results on honeycomb materials but also with results reported in the literature for microstructurally short cracks in metals.

Keywords: crack propagation, gradient-elasticity, digital image correlation, identification

1. Introduction

Since the pioneering works in (1), (2), (3), (4) and many others, Linear Elastic Fracture Mechanics (LEFM) has been extensively and successfully used for analyzing crack propagation in brittle materials. Recent advances in numerical simulations, especially the eXtended Finite Element Method (X-FEM) (5; 6), allow one for simulating

Email address: julien.rethore@ec-nantes.fr (Julien Réthoré)
[1]Now at GEM, CNRS UMR 6183 CNRS / Ecole Centrale de Nantes / Université de Nantes

the propagation of 3D cracks of arbitrary geometry through out a complex structure under complex loading. However, some situations remain difficult to model theoretically and numerically. This is the case for example of microstructurally short cracks. Whereas, this situation has been also extensively studied especially under cyclic loading, the strong influence of the material microstructure on the propagation of the crack is difficult to account for. Unless using recent 3D imaging technique it has been possible to obtain rich 3D data sets (7; 8), modelling such complex situation is still a difficult problem.

One may emphasize that two main phenomena are involved in these regime when the crack has strong interactions with the surrounding structure of the material. First, a directionality effect has to be considered. It results from the fact that the material structure does not allow the crack to grow in any direction. At the scale of the material structure, preferential crack orientations such as defined by slip systems or weak crystallographic planes exist. They define a few angles that the crack is allowed to follow. This has recently been accounted for within the context of a phase field model by introducing a penalization of the driving fracture energy within a predefined set of plane orientation (9). In (10), the directionality effect is inherited from the constitutive model, namely crystal plasticity. The second effect is called a size effect latter on. The strong interactions between a crack and the surrounding material structure are expected to be predominant while the crack length is of the same order of magnitude as the typical size of the material structure heterogeneity. Increasing the size of the crack then gives rise to an autonomous singular strain/stress field at the crack front which becomes the predominant driving mechanism of crack propagation. As soon as the autonomous nature of the crack tip field is established and the non-linear process zone remains confined, LEFM is the model suitable for describing crack propagation even in cases when, as mentioned before, crack shape, structure geometry and loading

are complex. The modelling scale in the approaches proposed in (9) and (10), is the scale of the material heterogeneity. This choice makes these models able to account for the influence of the material structure on crack propagation during the early stages of growth. However, these models are limited to small samples due to the numerical cost inherent from the modelling of material at such a small scale. Consequently, the situation when LEFM is appropriate will never be met with these models.

In this paper, the case of honeycomb materials is considered as a model case for analyzing the interactions between a crack and the material structure. Based on the experimental analysis of the displacement of such materials, it was proposed in a previous paper to use gradient-elasticity (11) as a continuum model. Due to its second order energy term, internal lengths arise from this formulation and they play an important role for capturing the effects of the micro-structure. Using this model and taking benefit of its internal lengths, it is possible to start with small cracks being under the influence of the material structure and then to have them gaining their autonomous nature when increasing their lengths. It will thus be possible to capture the aforementioned size effect using gradient-elasticity. Concerning directionality, it should be possible to introduce a fracture energy that depends on the local crack orientation (12). Herein, it is preferred to transfer the macroscopic kinematic variables at the crack tip to the microscopic scale. At this scale a representative volume element is considered and the crack propagation angle is estimated from the mechanical state of this volume under a loading inherited from the macroscopic kinematic variables. First, in Section 2, some experimental results of crack propagation in honeycomb materials are presented. In Section 3, the gradient-elasticity framework and its numerical implementation for introducing cracks is detailed. The failure criterion from which directionality arises is described in Section 4. Then, in Section 5, results obtained with the proposed framework are presented. It is demonstrated that directionality and size effects are captured

and that numerical results compare well with experiments performed on model architectured materials.

2. Experimental observation

Failure experiments on honeycomb materials have been performed. The specimen geometry is defined in Figure 1. The left arms of the specimen are fixed in the grips of a standard tensile device and submitted to a constant vertical displacement speed of 0.1mm/min. The specimens were obtained by a 3D printer. They are made from photosensitive ABS-type polymer powder. The bulk material obtained from this process is isotropic. Its elastic behaviour is defined by a Young's modulus of 1.4 GPa and a Poisson's ratio of 0.4. A pre-crack has been designed by simply not printing some cells along the symmetry plane of the specimen. The results presented in this paper are based on the analysis of a material generated by a periodic tilling of the D_2 cell presented in Figure 2. This cell is invariant by rotation of $2\pi/2$. It is also invariant by symmetry with respect to horizontal and vertical planes. The edges are 140 μm thick and 1100 μm long. The material is therefore orthotropic for first order elasticity. For this unit cell geometry, experiments until rupture have been carried out. Two orientations (0^o and 90^o) of the material structure with respect to the specimen axis are tested. The crack paths are shown in Figure 3 and they clearly show how the material orientation can influence failure in such material. A closer view of the broken cells is presented in Figure 4. From these experimental observations, it appears that, at the microscopic scale, failure occurs at the corners of the unit cells. This observation holds for all the unit cell geometries tested experimentally. Consequently, it is mandatory to incorporate the topology of the unit cell in the crack angle criterion.

3. Gradient-elasticity: theoretical background and numerical elaboration

3.1. Formulation

To fulfill the requirements established from the experimental analysis in (11), the modeling of the macroscopic continuum describing the behaviour of the honeycomb material must incorporate strain gradient as a kinematic variable. Within the framework proposed in (13), $\underset{\sim}{\mathbf{E}}$, the symmetric gradient of the displacement $\underline{\mathbf{U}}$, and $\underset{\approx}{\kappa}$, the gradient of $\underset{\sim}{\mathbf{E}}$, are chosen as the descriptors of the kinematic of the continuum:

$$\underset{\sim}{\mathbf{E}} = \frac{1}{2}(\underline{\nabla}_{\underline{\mathbf{X}}}\,\underline{\mathbf{U}} + \underline{\nabla}^{T}_{\underline{\mathbf{X}}}\,\underline{\mathbf{U}}) = \underline{\nabla}^{s}_{\underline{\mathbf{X}}}\,\underline{\mathbf{U}} \qquad\qquad \underset{\approx}{\kappa} = \underline{\nabla}_{\underline{\mathbf{X}}}\,\underset{\sim}{\mathbf{E}}. \tag{1}$$

Using index notation, this is rewritten as

$$E_{ij} = \frac{1}{2}(U_{i,j} + U_{j,i}) \qquad\qquad \kappa_{ijk} = E_{ij,k} = \frac{1}{2}(U_{i,jk} + U_{j,ik}). \tag{2}$$

The strain energy density Ψ subsequently depends on these two kinematic variables, $\Psi = \Psi(\underset{\sim}{\mathbf{E}}, \underset{\approx}{\kappa})$. The classical Cauchy stress and the hyper-stress are then defined as

$$\underset{\sim}{\mathbf{\Sigma}} = \frac{\partial \Psi}{\partial \underset{\sim}{\mathbf{E}}} \qquad\qquad \underset{\approx}{\mathbf{S}} = \frac{\partial \Psi}{\partial \underset{\approx}{\kappa}}. \tag{3}$$

Under the assumption that there is no coupling between first and second order terms and no energy associated to the rotation, the following expression for Ψ is obtained:

$$\Psi(\underset{\sim}{\mathbf{E}}, \underset{\approx}{\kappa}) = \frac{1}{2}\underset{\sim}{\mathbf{E}} : \underset{\sim}{\mathbf{\Sigma}} + \frac{1}{2}\underset{\approx}{\kappa} \vdots \underset{\approx}{\mathbf{S}}. \tag{4}$$

The behaviour of such a continuum thus relies on two constitutive linear operators. The first order elastic tensor $\underset{\approx}{\mathbf{C}}$ which establishes the linear relationship between stress and strain reads

$$\underset{\sim}{\mathbf{\Sigma}} = \underset{\approx}{\mathbf{C}} : \underset{\sim}{\mathbf{E}}, \qquad i.e. \qquad \Sigma_{ij} = C_{ijkl} E_{kl}, \tag{5}$$

and the second order elastic tensor $\underset{\approx}{\underset{\approx}{\mathbf{A}}}$ which plays the same role for the hyper-stress and the strain gradient:

$$\underset{\simeq}{\mathbf{S}} = \underset{\approx}{\underset{\approx}{\mathbf{A}}} \vdots \underset{\simeq}{\boldsymbol{\kappa}}, \qquad i.e. \qquad S_{ijk} = A_{ijklmn}\kappa_{lmn}. \tag{6}$$

In 2D, due to symmetry considerations, the number of material constants in $\underset{\approx}{\mathbf{C}}$ reduces to 6 in the fully anisotropic case. In this context, for $\underset{\approx}{\underset{\approx}{\mathbf{A}}}$, the maximum number of material constants is 21. In a simplified version, it is proposed in (14) to use only one additional parameter. Due to the anisotropy of the material considered hereafter, while the proposition by (15) could have been adopted, it is preferred to keep the general form of these relations. Based on the analysis of the material symmetry as proposed in (16), the class of anisoptropy of the constitutive operators can be derived and their intrinsic form is established with the lowest number of parameters. In (16), it is also proposed to estimate numerically the first and second order elastic tensors. However, the homogenization technique used in the latter is purely kinematic which is known to lead to overestimated stiffness. Herein, we chose the periodic homogenization scheme proposed in (17) to derived the macroscopic elastic tensors $\underset{\approx}{\mathbf{C}}$ and $\underset{\approx}{\underset{\approx}{\mathbf{A}}}$ as described in the next section.

3.2. Effective properties

The second order computational homogenization scheme proposed in (17) is used to estimate the effective first order and second order elastic behaviour of the honeycomb materials. The first ingredient of the scheme consists in the boundary conditions applied to the unit cell. The microscopic displacement $\underline{\mathbf{u}}$ is supposed to be the sum of the displacement inherited from the macroscopic scale plus an unknown additionnal fluctuation $\underline{\mathbf{w}}$ that is further assumed to be periodic:

$$\underline{\mathbf{u}}(\underline{\mathbf{x}}) = \underset{\sim}{\mathbf{E}}.\underline{\mathbf{x}} + \frac{1}{2}\underline{\mathbf{x}}.\underset{\simeq}{\boldsymbol{\kappa}}.\underline{\mathbf{x}} + \underline{\mathbf{w}}(\underline{\mathbf{x}}). \tag{7}$$

In this equation, $\underset{\sim}{\mathbf{E}}$ is the macroscopic strain, $\underset{\simeq}{\kappa}$ its gradient and $\underline{\mathbf{x}}$ the position of any point in the unit cell calculated in the local unit cell coordinates system. Let us define $\underline{\mathbf{x_A}}$ and $\underline{\mathbf{x_B}}$ as the location of two homologous points along the unit cell boundary in the unit cell coordinates system. As periodicity is assumed ($\underline{\mathbf{w}}(\underline{\mathbf{x_A}}) = \underline{\mathbf{w}}(\underline{\mathbf{x_B}})$), the following relationship is established:

$$\underline{\mathbf{u}}(\underline{\mathbf{x_A}}) - \underline{\mathbf{u}}(\underline{\mathbf{x_B}}) = \underset{\sim}{\mathbf{E}}.(\underline{\mathbf{x_A}} - \underline{\mathbf{x_B}}) + \frac{1}{2}\underline{\mathbf{x_A}}.\underset{\simeq}{\kappa}.\underline{\mathbf{x_A}} - \frac{1}{2}\underline{\mathbf{x_B}}.\underset{\simeq}{\kappa}.\underline{\mathbf{x_B}} \tag{8}$$

As shown in (17), the equality between the macroscopic strain $\underset{\sim}{\mathbf{E}}$ and the average of the microscopic strain is fulfilled intrinsically. Conversely, one has to further constrain the displacement along the unit cell boundary in order to ensure that this equality holds between the macroscopic strain gradient $\underset{\simeq}{\kappa}$ and its microscopic average. For this purpose, it is prescribed that the average microscopic periodic fluctuation $\underline{\mathbf{w}}$ along each edge C of the unit cell vanishes:

$$\int_{A\in C} \underline{\mathbf{w}}(\underline{\mathbf{x_A}})\mathrm{d}s = \underline{\mathbf{0}}\,. \tag{9}$$

This additional constraint is prescribed for only half of the edges of the unit cell, the constraint being automatically satisfied for the homologous edges due to periodicity. Using the mesh presented in Figure 5, elastic simulations of the unit cell under this boundary condition for 9 independent elementary loading are performed (3 for each component of $\underset{\sim}{\mathbf{E}}$ and 6 for each component of $\underset{\simeq}{\kappa}$). From the results of these simulations, the average of the microscopic stress $\underset{\sim}{\boldsymbol{\sigma}}$ and its first moment are computed over the unit cell surface $\mathcal{S}$:

$$< \underset{\sim}{\boldsymbol{\sigma}} >= \frac{1}{meas(\mathcal{S})} \iint_{\mathcal{S}} \underset{\sim}{\boldsymbol{\sigma}} \mathrm{d}S \qquad\qquad < \underset{\sim}{\boldsymbol{\sigma}}\,\underline{\mathbf{x}} >= \frac{1}{meas(\mathcal{S})} \iint_{\mathcal{S}} \underset{\sim}{\boldsymbol{\sigma}}\,\underline{\mathbf{x}}\,\mathrm{d}S. \tag{10}$$

Then using the generalization of the Hill-Mandel theorem, the effective first and second order elastic tensors are estimated. For the material analyzed herein which is supposed to be isotropic at the microscopic scale with the elastic parameters as defined in

Section 2, the following results are obtained:

$$\begin{bmatrix} \Sigma_{11} \\ \Sigma_{22} \\ \Sigma_{12} \end{bmatrix} = \begin{bmatrix} 420 & 40 & 0 \\ 40 & 180 & 0 \\ 0 & 0 & 30 \end{bmatrix} \begin{bmatrix} E_{11} \\ E_{22} \\ E_{12} \end{bmatrix} \tag{11}$$

and

$$\begin{bmatrix} S_{111} \\ S_{221} \\ S_{122} \\ S_{222} \\ S_{112} \\ S_{122} \end{bmatrix} = \begin{bmatrix} 2 & 1 & -9 & 0 & 0 & 0 \\ 1 & 79 & -3 & 0 & 0 & 0 \\ -9 & -3 & 31 & 0 & 0 & 0 \\ 0 & 0 & 0 & 75 & 22 & -21 \\ 0 & 0 & 0 & 22 & 225 & -6 \\ 0 & 0 & 0 & -21 & -6 & 6 \end{bmatrix} \begin{bmatrix} \kappa_{111} \\ \kappa_{221} \\ \kappa_{122} \\ \kappa_{222} \\ \kappa_{112} \\ \kappa_{122} \end{bmatrix}. \tag{12}$$

These results are given in the unit cell coordinates system for a unit cell orientation as in Figures 2 and 3(a). The unit are MPa for first order (Equation (11)) and MPa.mm^2 for second order (Equation (12)).

3.3. Discretization

In order to incorporate the crack into the macroscopic numerical model, a discretization scheme based on X-FEM (18) is developed. It is chosen here to use the displacement field as the only unknown field for the discrete problem. It subsequently implies that the discretization has C^1 continuity. The C^1 triangular element proposed in (19) is used for this purpose. In this element, each node holds 6 shape functions which corresponding unknowns are the discrete field, its two first order derivatives and its three second order derivatives at the nodal position as detailed in the Appendix of the paper. Each component i of the displacement is approximated as follows:

$$U_i(\underline{\mathbf{X}}) = \sum_{n \in \mathcal{N}} \sum_{k=1..6} \phi_n^k(\underline{\mathbf{X}}) \bar{u}_{ink}. \tag{13}$$

In this equation, $\mathcal{N}$ is the set of nodes in the triangulation of the discretized domain Ω, $(\phi_n^k)_{k=1..6}$ the shape functions for each node and $(\bar{u}_{ink})_{k=1..6}$ the corresponding unknowns for the i^{th} component of the displacement. For introducing an enrichment to the approximation space that captures the influence of the crack, we use the shifted Heaviside enrichment from (20). This discontinuous enrichment allows to maintain the same degree of continuity as for the shape functions supporting the enrichment over the so-called blending elements (elements that have not all their nodes enriched). Compared to the original discontinuous enrichment proposed in (5), the shifted enrichment does not change the solution, it leads to a different implementation of the method. Concerning the asymptotic singular enrichment originally used in the X-FEM, it is required that the order of the singularity at the crack tip is known. In the gradient-elasticity framework, there is no general solution for the asymptotic fields except in a few specific cases (21; 22). We thus make use of the discontinuous enrichment only. The enriched approximation is then written as:

$$U_i(\underline{\mathbf{X}}) = \sum_{n\in\mathcal{N}}\sum_{k=1..6} \phi_n^k(\underline{\mathbf{X}})\bar{u}_{ink} + \sum_{n\in\mathcal{N}_d}\sum_{k=1..6} \phi_n^k(\underline{\mathbf{X}})(\mathcal{H}(\underline{\mathbf{X}}) - \mathcal{H}(\underline{\mathbf{X}}_{\mathbf{n}}))\tilde{u}_{ink}, \qquad (14)$$

where $\mathcal{N}_d$ is the set of enriched nodes, those which support is cut by the crack, and $\mathcal{H}$ the Heaviside jump function which value jumps from 0 below to 1 above the crack. This discontinuous enrichment is shifted by the value of the Heaviside function at the corresponding nodal position $\underline{\mathbf{X}}_{\mathbf{n}}$. $(\tilde{u}_{ink})_{k=1..6}$ are the additional degrees of freedom.

From the strain energy density defined in Equation (4) and the approximation defined by Equation (14), the discretized weak form of the balance equations is elaborated. It recasts as a linear system of equations. The numerical integration is performed using usual Gauss quadrature for the standard elements and a quadrature rule using non-conforming sub-cells for the enriched elements.

4. Failure criteria

4.1. Crack angle criterion

From the experimental observations presented in Section 2, it is concluded that the crack cannot follow an arbitrary path in periodic honeycomb materials. Only a finite number of crack directions is allowed depending on the symmetry class of the material. This set of possible crack orientations is the analogous of the slip systems used in the crystal plasticity theory. When going through a cell, the crack can only go from one nucleation point to one of its homologous points (these points being at the position of that nucleation point in the neighboring cells). As the material structure is periodic, it is though that failure also obeys this periodicity. So any orientation that is not defined by joining two homologous points of the unit cell is not admissible. For the considered unit cell geometry, the possible crack orientations are plotted using red lines in Figure 2. In the spirit of the homogenization theory, a unit cell supposed to be located just in front of the crack tip is loaded using the macroscopic kinematic variables. Macroscopic average estimates of the first and second derivatives of the displacement are transferred to the microscopic scale as Dirichlet conditions along the boundary of the unit cell. Each component of the microscopic displacement u_i is thus derived along the unit cell boundary using the following equation:

$$u_i = \bar{U}_{i,j}\, x_j + \frac{1}{2}\bar{U}_{i,jk}\, x_j\, x_k. \tag{15}$$

In this equation, $\bar{U}_{i,j}$ are the average tip estimates of first order macroscopic displacement derivatives, $\bar{U}_{i,jk}$ the average tip estimates of its second order derivatives and x_j the coordinates of the points along the unit cell boundary in the local microscopic coordinates system. Note that due to the second order term in the energy, the strain singularity should vanish at the crack tip. Further, the average estimates of the displacement derivatives which are used to tranfert the kinematic variables from the macroscopic

scale to the unit cell, are not supposed to be infinite. This will be detailled and illustrated in Section 4.2.

An elastic FE simulation of the unit cell under this loading inherited from the macroscopic scale is performed using the mesh depicted in Figure 5. From the results of this simulation, the generalized stress intensity factors B_I and B_{II} at the v-notches of the cell corners are computed using a path independent integral (23; 24). A brief overview of the technique is presented in the Appendix of the paper. The integration contours for this integral are the boundary of the refined zone around each corner as presented in Figure 5. Considering mode I and mode II, the corner submitted to the maximum value of an equivalent generalized stress intensity factor

$$B_{eq} = \sqrt{B_I^2 + B_{II}^2} \tag{16}$$

is searched for. Once the most loaded corner is detected the nucleation point is set. Then the crack orientation is defined by the line going from the nucleation point to its homologous point having the highest equivalent generalized stress intensity factor B_{eq}.

4.2. Tip Averaging

The procedure described above requires the evaluation of reliable estimates of the first and second derivatives of the displacement at the crack tip. At the macroscopic scale, these quantities may have a singular behaviour. A non-local estimate is thus required. The average value of these quantities over a disc centered at the crack tip is adopted in the sequel. The size of the averaging domain is equal to the unit cell size l_c.

For the evaluation of fracture criteria, non-local estimates of the stress tensor have been extensively used in the simulation of the crack propagation using X-FEM (25). This technique does not provide a reliable estimate of the stress amplitude at the crack tip and a calibration procedure of the critical nucleation stress is to be considered for

a given mesh size. However, the crack angle is correctly predicted as all the stress components are affected by the same approximation.

For using this kind of non-local tip averaging, a new challenge arises in the context of gradient elasticity. Indeed, it is known that the second order term in the energy density has the effect of cancelling the singularity of the strain field at the crack tip (21; 22). Further, for transferring to the microscopic scale reliable boundary conditions based on estimates of the displacement derivatives (see Equation (15)), the actual weighting between strain (vanishing at the crack tip) and strain gradient (singular) over the averaging domain must be captured accurately. This is not possible using standard non-local field estimates which reveal all the more so inconvenient that the averaging domain size (fixed to the size of the unit cell) may ideally be lower or of the order of the finite element mesh size.

The idea we develop is based on a homogeneous decomposition of the displacement field. Each component of $\underline{\mathbf{U}}$ is written as:

$$U_i = f(r)g(\theta), \tag{17}$$

(r,θ) being the local polar coordinates and f, g scalar functions. Note that the asymptotic solutions given in (21) for a fully isotropic material have this property. Considering a circular domain around the crack tip, one can easily obtain f, respectively g, by averaging U_i with respect to θ, respectively r. This is illustrated in Figure 6. The other assumption is that f is a power law, $\beta_i r^{\alpha_i}$, which exponent is obtained by linear regression of f in log-log scale. β_i is then obtained so that the average value of U_i equals the average value of $\beta_i r^{\alpha_i} g(\theta)$. The domain average of the first and second displacement derivatives are transformed into contour integrals, by using the divergence theorem, invoking the displacement and its first derivative. The latter are computed from the semi-analytic formula (17). Thanks to this semi-analytical formula, reliable

non-local estimates of the displacement derivatives are obtained even for small averaging domain size compared to the finite element mesh size, the estimation of f and g being performed on circular domain larger than l_c. For illustration purposes, the value of the average value $\bar{U}_{y,y}$ and $\bar{U}_{y,yx}$ of $U_{y,y}$ and $U_{y,yx}$ are plotted as functions of the averaging domain size in Figure 7. The typical asymptotic behaviour is retrieved in this case when the exponent of the power law is higher than 1.

5. Examples

5.1. Numerical setup

A rectangular specimen of 60×120 mm is considered. An initial crack of length $a = 60$ mm is defined. It is horizontal and it cuts the specimen along its symmetry axis. The initial crack tip position is right in the center of the specimen. The top and bottom left corners have their vertical displacement prescribed so that opening of the crack occurs. The value of the prescribed displacement amplitude is arbitrary, only the crack path being tracked for. In this configuration, for an homogeneous elastic material, the crack grows straight through the specimen. The mesh used for the numerical simulation is shown in Figure 8. The element size h is about 0.03 times the initial crack length a. The domain size for estimating f and g (see Section 4.2) is equal to h whereas the averaging domain size is fixed to the unit cell size l_c. The latter is set to the radius of the circle passing through the inner corners of the unit cell which geometry was defined in Secion 2. Between two successive time steps, the crack is supposed to grow by an increment $da = h$.

Some of the results we obtained are first described before the anisotropy to failure and size effects are analyzed in more details.

5.2. Results

The normalized vertical displacement field at the end of the computations is shown in Figure 9(b). The case considered in this Figure is the D_2 material rotated by $\alpha = \frac{\pi}{2}$ (see Figure 3(b)). It is observed that the enrichment allows to capture the discontinuity and that the crack path is not smooth. Due to the interactions between the crack and the surrounding micro-structure the crack orientation oscillates leading to zig-zag patterns. Note that it has been checked that this is not an effect of the finite crack length increment da, the steps in the crack path presented in Figure 9(b) being longer than da.

To illustrate the two-scale criterion for the crack angle, the deformed unit cell at the crack tip is depicted in Figure 10 for the first step of the analyses with an amplification factor of 100. The L_2 norm of the strain field is plotted in this Figure.

5.3. Anisotropy & Size effects

First, the influence of the unit cell orientation α is analyzed. The crack paths obtained for α varying in the range defined above are shown in Figure 11. The effect of α is not smooth. Due to the discrete nature of the crack angle criterion (only a finite number of orientation being admissible), it appears that the crack selects a path among a limited number of admissible orientations. This is especially pronounced in Figure 11 where only four paths are followed by the crack. This demonstrates the ability of the proposed failure criterion to account for the directionality effect due to the influence of the micro-structure at the macroscopic scale. However, this results from a competition of the discrete crack angle criterion and the gradient-elasticity macroscopic model. To further analyze this competition, the unit cell size is decreased by a factor of 10. The ratio between the unit cell size l_c and the initial crack length a is subsequently decreasing from 0.013 to 0.0013. The results are presented in Figures 9(c)

and 12. The crack paths are almost rectilinear and it is now observed that the overall crack orientation varies continuously with the unit cell orientation α (see Figure 12). The contribution of the second order term in the strain energy density being 100 times lower, the anisotropy to failure only lies on the anisotropy of the first order elastic tensor and on the discrete nature of the crack angle criterion. Indeed, only two opposite orientations are allowed for this unit cell geometry (see Figure 4) but they change continuously with the variation of the unit cell orientation α. For this unit cell size, the crack is driven by the singularity of the strain field has shown in Figure 13(b). This singularity has an autonomous character and it is not influenced by structural effects.

For a fixed orientation of $\alpha = \frac{\pi}{2}$, the unit cell size is now varied within a larger range. A 10 times larger unit cell is considered as well as an infinitely small unit cell. This configuration is obtained by cancelling the contribution of the second order energy term ($\underset{\approx\approx}{\mathbf{A}} = 0$). The results are presented in Figure 14. Decreasing the unit cell size ($l_c/a = 0.0013$), the crack paths is similar to the result obtained for the infinitely small unit cell ($l_c/a = 0$). This demonstrate how the gradient-elasticity model progressively decreases the influence of the material structure at the macroscopic scale for smaller and smaller cells until the results become identical to the result of classical first order elasticity.] As shown in Figure 13(a), the strain field for large cells loses its singular nature. This means that the strain and gradient of strain used to load the unit cell at the crack tip with the proposed failure criterion arises from a displacement field having an exponent n larger than 1. Such a displacement field is more influenced by structural effects than when $n \leq 1$. This results in a global orientation of the crack (horizontal in the present case as shown in Figures 14 and 9(a) for $l_c/a = 0.13$) that is inherited from the geometry of the specimen and its boundary conditions. Because this crack orientation is not allowed by the unit cell symmetry, a zig-zag pattern is obtained. The proposed model is thus capable of capturing the influence of the material structure at

the macroscopic scale: directionality and size effect are obtained. The first effect results from the discrete nature of the crack angle criterion and from the anisotropy of the elastic behaviour of the material. The size effect is induced by gradient-elasticity that changes the mechanical fields around the crack tip.

6. Conclusion

In this paper, a fracture mechanics gradient-elasticity framework is elaborated. An original contribution of the paper is that an X-FEM numerical framework is proposed for gradient-elasticity. Then, a crack angle criterion is proposed based on a transfer of non-local tip estimates of the macroscopic kinematic variables to the microscopic scale. The proposed criterion accounts for the existence of only a few possible crack orientations by analogy to crystal plasticity. The discrete character of the criterion allows for capturing a directionality effect as observed experimentally. Gradient-elasticity introduces a length scale which balances the effect of the material structure heterogeneity at the macroscopic scale. By increasing the size of the unit cell of the material, or by decreasing the size of the initial crack, the contribution of second order terms strongly modifies the mechanical fields. As a consequence, the crack path is also affected by this size effect. Zig-zag crack patterns as observed in actual monocrystalline alloys are reproduced.

The framework is validated using experiments performed on model architectured materials but, there is no limitation to use the proposed model for more complex material structures.It may thus have the ability to capture the strong interactions between a crack and the material structure in cases when the material structure is polycrystalline, the problem is 3D and the crack geometry is a complex 3D surface. The proposed methodology opens a new way for handling the complex question of the propagation of short cracks. Further, the model is based on a macroscopic continuum model what

a priori makes possible the analysis of structural components.

Acknowledgements

This work was partially supported by SAFRAN-AREVA-INSA chair fundings. The support of Pays de la Loire, through grant MatSyMat, labelled by EMC2, is also gratefully acknowledged.

7. APPENDIX A: Generalized Stress Intensity Factors estimation

The methodology used for the estimation of generalized stress intensity factors $B_{I,II}$ is proposed in (24). The domain of interest $\mathcal{D}$ for the analysis is located at the vicinity of a notch of angle ω as defined in Figure 15. Following (24), the displacement around the notch as a function of the distance to the notch tip r and the angle θ with respect to the symmetry axis of the notch $\underline{\mathbf{e_1}}$ is supposed to write

$$\underline{\mathbf{u}}(r,\theta) = \sum_{i\in[I,II]} B_i r^{\alpha_i}(H_1(\alpha_i)\underline{\psi_1}(\theta,\alpha_i) + H_2(\alpha_i)\underline{\psi_2}(\theta,\alpha_i). \tag{18}$$

In this equation, H_1, H_2 are geometry functions, $\underline{\psi_1}, \underline{\psi_2}$ elementary solutions and $(\alpha_i)_{i\in[I,II]} > 1$ the solutions of the characteristic equations

$$\sin(\alpha_I\omega) - \alpha_I \sin(\omega) = 0 \tag{19}$$

and

$$\sin(\alpha_{II}\omega) + \alpha_{II} \sin(\omega) = 0 \tag{20}$$

defining the two modes. H_1, H_2 are given by:

$$H_1(\alpha) = (\alpha-1)\sin\big((\alpha+1)\omega\big) - (\alpha+1)\sin\big((\alpha-1)\omega\big) \tag{21}$$

and

$$H_2(\alpha) = -(\alpha+1)\Big[\cos\big((\alpha+1)\omega\big) - \cos\big((\alpha-1)\omega\big)\Big]. \tag{22}$$

The elementary solutions are defined as follows:

$$\underline{\psi_1}(\alpha,\theta) = \begin{pmatrix} (\lambda+\mu)\alpha\cos((\alpha-2)\theta) - \Big((\lambda+\mu)(\alpha+2)+2\mu\Big)\cos(\alpha\theta) \\ -(\lambda+\mu)\alpha\sin((\alpha-2)\theta) - \Big((\lambda+\mu)\alpha-2\mu\Big)\sin(\alpha\theta) \end{pmatrix} \tag{23}$$

$$\underline{\psi_2}(\alpha,\theta) = \begin{pmatrix} (\lambda+\mu)\alpha\sin((\alpha-2)\theta) - \Big((\lambda+\mu)(\alpha+2)+2\mu\Big)\sin(\alpha\theta) \\ (\lambda+\mu)\alpha\cos((\alpha-2)\theta) - \Big((\lambda+\mu)\alpha-2\mu\Big)\cos(\alpha\theta) \end{pmatrix} \tag{24}$$

where λ,μ are the Lamé coefficients of the homogeneous isotropic material in the considered domain $\mathcal{D}$.

Then, Betty's theorem is used over a domain $\mathcal{D}^R_{r_0}$ defined by $\{(r,\theta)|r_0 \leq r \leq R, 0 \leq \theta \leq \omega\}$. If $\underline{\tilde{\mathbf{u}}}$ denotes an auxiliary displacement field satisfying the balance of momentum equation, then the following equality holds:

$$\int_{\mathcal{D}^R_{r_0}} \Big(\underset{\sim}{\boldsymbol{\Sigma}}(\underline{\mathbf{u}}) : \underset{\sim}{\mathbf{E}}(\underline{\tilde{\mathbf{u}}}) - \underset{\sim}{\boldsymbol{\Sigma}}(\underline{\tilde{\mathbf{u}}}) : \underset{\sim}{\mathbf{E}}(\underline{\mathbf{u}})\Big) dx = \int_{\Gamma_{r_0}\cup\Gamma_R} \Big(\underset{\sim}{\boldsymbol{\Sigma}}(\underline{\mathbf{u}}).\underline{\mathbf{n}}.\underline{\tilde{\mathbf{u}}} - \underset{\sim}{\boldsymbol{\Sigma}}(\underline{\tilde{\mathbf{u}}}).\underline{\mathbf{n}}.\underline{\mathbf{u}}\Big) ds = 0 \tag{25}$$

If $(\alpha_i)_{i\in[I,II]}$ are the solution of the characteristic equations 19 and 20, then $(-\alpha_i)_{i\in[I,II]}$ are also solutions of these equations. The solutions for these values of α have a non physical behaviour as the strain energy density is singular. However, these solutions fulfill the conditions for being used in the Betty's theorem and they allow to extract from a given displacement field the corresponding B_i. Indeed, for a given mode, if $\underline{\tilde{\mathbf{u}}}$ equals $r^{-\alpha_i}(H_1(-\alpha_i)\underline{\psi_1}(\theta,-\alpha_i) + H_2(-\alpha_i)\underline{\psi_2}(\theta,-\alpha_i) = r^{-\alpha_i}\,\underline{\tilde{\mathbf{v}}}$ and $\underline{\mathbf{u}}$ is assumed to decompose as in Equation (18) then taking the limit when r_0 vanishes, Betty's theorem leads to the following relationship:

$$A(\alpha_i)B_i = \int_{\Gamma_R} \Big(\underset{\sim}{\boldsymbol{\Sigma}}(\underline{\mathbf{u}}).\underline{\mathbf{n}}.\underline{\tilde{\mathbf{u}}} - \underset{\sim}{\boldsymbol{\Sigma}}(\underline{\tilde{\mathbf{u}}}).\underline{\mathbf{n}}.\underline{\mathbf{u}}\Big) ds \tag{26}$$

where

$$\begin{aligned} A(\alpha) = \int_0^\omega \Big\{ \Big[\big(\gamma_1\tilde{E}_{11} + \gamma_2\tilde{E}_{22}\big)\cos(\theta) + 2\mu\tilde{E}_{12}\sin(\theta)\Big]\tilde{v}_1 + \\ \Big[2\mu\tilde{E}_{12}\cos(\theta) + \big(\gamma_1\tilde{E}_{22} + \gamma_2\tilde{E}_{11}\big)\sin(\theta)\Big]\tilde{v}_2 \Big\} d\theta \end{aligned} \tag{27}$$

and

$$\gamma_1 = 2\mu\Big(\frac{1}{\lambda+2\mu}+1\Big), \quad \gamma_2 = \frac{2\mu}{\lambda+2\mu}. \tag{28}$$

In these equations, $\tilde{E}_{ij}$ are such that

$$E_{ij}(r^{\alpha_i}(H_1(\alpha_i)\underline{\psi_1}(\theta,\alpha_i)+H_2(\alpha_i)\underline{\psi_2}(\theta,\alpha_i)) = r^{\alpha_i-1}\tilde{E}_{ij} \tag{29}$$

The B_i coefficients are thus computed by evaluating a contour integral involving the actual displacement field and an auxiliary displacement and the integral of analytical functions $A(\alpha)$.

8. APPENDIX B: C^1 shape functions for triangular elements

In this Appendix, the equations for computing the C^1 shape functions for a 3-node triangular element as given in (19) are detailed. Each node of the triangle holds 6 shape functions which corresponding degrees of freedom are the discretized field and its first and second derivatives. As usual for triangular 3-node elements, the expressions for the shape functions use the area coordinates L_i which are related to the rectangular coordinates of the evaluation point x, y and those of each nodes of the triangle x_i, y_i, for i between 1 and 3. The following relationships hold:

$$L_i = \frac{a_i + b_i x + c_i y}{2\Delta}, \tag{30}$$

$$x = L_1 x_1 + L_2 x_2 + L_3 x_3 \tag{31}$$

and

$$L_1 + L_2 + L_3 = 1. \tag{32}$$

In the first equation, Δ is the area of the element and a_i, b_i, c_i constant parameters given by

$$a_i = x_j y_k - x_k y_j,\ b_i = y_j - y_k,\ c_i = x_k - x_j, \tag{33}$$

i, j, k being the cyclic permutation of 1,2 and 3. Then, the 6 shape functions for node i are:

$$
\begin{aligned}
N_1 &= L_1^5 + 5L_1^4L_2 + 5L_1^4L_3 + 10L_1^3L_2^2 + 10L_1^3L_3^2 + 20L_1^3L_2L_3 + 30r_{21}L_1^2L_2L_3^2 + 30r31L_1^2L_3L_2^2 \\
N_2 &= c_3L_1^4L_2 - c_2L_1^4L_3 + 4c_3L_1^3L_2^2 - 4c_2L_1^3L_3^2 + 4(c_3 - c_2)L_1^3L_2L_3 - (3c_1 + 15r_{21}c_2)L_1^2L_2L_3^2 + (3c_1 + 15r_{31}c_3)L_1^2L_3L_2^2 \\
N_3 &= -b_3L_1^4L_2 + b_2L_1^4L_3 - 4b_3L_1^3L_2^2 + 4b_2L_1^3L_3^2 + 4(b_2 - b_3)L_1^3L_2L_3 + (3b_1 + 15r_{21}b_2)L_1^2L_2L_3^2 - (3b_1 + 15r_{31}b_3)L_1^2L_3L_2^2 \\
N_4 &= 0.5c_3^2L_1^3L_2^2 + 0.5c_2^2L_1^3L_3^2 - c_2c_3L_1^3L_2L_3 + (c_1c_2 + 5/2r_{21}c_2^2)L_2L_3^2L_1^2 + (c_1c_3 + 5/2r_{31}c_3^2)L_3L_2^2L_1^2 \\
N_5 &= -b_3c_3L_1^3L_2^2 - b_2c_2L_1^3L_3^2 + (b_2c_3 + b_3c_2)L_1^3L_2L_3 - (b_1c_2 + b_2c_1 + 5r_{21}b_2c_2)L_2L_3^2L_1^2 - (b_1c_3 + b_3c_1 + 5r_{31}b_3c_3)L_3L_2^2L_1^2 \\
N_6 &= 0.5b_3^2L_1^3L_2^2 + 0.5b_2^2L_1^3L_3^2 - b_2b_3L_1^3L_2L_3 + (b_1b_2 + 5/2r_{21}b_2^2)L_2L_3^2L_1^2 + (b_1b_3 + 5/2r_{31})b_3^2L_3L_2^2L_1^2
\end{aligned}
\tag{34}
$$

where $r_{ij} = \frac{b_ib_j + c_ic_j}{b_i^2 + c_i^2}$. One obtains the shape functions for the other two nodes by cyclic permutation of the indices of a, b, c, L and r

References

[1] G. Irwin, Analysis of stress and strains near the end of a crack traversing a plate, Journal of Applied Mechanics 24 (3) (1957) 361–364.

[2] J. Rice, A path independant integral and the approximate analysis of strain concentration by notches and cracks, Journal of Applied Mechanics 35 (1968) 379–386.

[3] G. Barenblatt, The mathematical theory of equilibrium cracks in brittle fracture, Advances in Applied Mechanics 7 (1962) 55–126.

[4] M. Williams, On the stress distribution at the base of a stationary crack, ASME Journal Applied Mechanics 24 (1957) 109–114.

[5] N. Moës, J. Dolbow, T. Belytschko, A finite element method for crack growth without remeshing, International Journal for Numerical Methods in Engineering 46 (1) (1999) 133–150.

[6] N. Moës, A. Gravouil, T. Belytschko, Non-planar 3d crack growth by the extended finite element and level sets. part i: Mechanical model, International Journal for Numerical Methods in Engineering 53 (11) (2002) 2549–2568.

[7] P. Cloetens, M. Pateyron-Salomé, J. Buffiere, G. Peix, J. Baruchel, F. Peyrin, M. Schlenker, Observation of microstructure and damage in materials by phase sensitive radiography and tomography, Journal of Applied Physics 81 (9) (1997) 5878–5886.

[8] M. Herbig, A. King, P. Reischig, H. Proudhon, E. Lauridsen, J. Marrow, J. Buffière, W. Ludwig, 3-d growth of a short fatigue crack within a polycrystalline microstructure studied using combined diffraction and phase-contrast x-ray tomography, Acta Materialia 59 (2) (2011) 590–601.

[9] J. Clayton, J. Knap, Phase field modeling of directional fracture in anisotropic polycrystals, Computational Materials Science 98 (2015) 158–169.

[10] J. Li, H. Proudhon, A. Roos, V. Chiaruttini, S. Forest, Crystal plasticity finite element simulation of crack growth in single crystals, Computational Materials Science 94 (2014) 191–197.

[11] J. Réthoré, C. Kaltenbrunner, T. Dang, P. Chaudet, M. Kuhn, Gradient-elasticity for honeycomb materials: Validation and identification from full-field measurements, International Journal of Solids and Structures 72 (2015) 108–117.

[12] B. Li, C. Peco, D. Millán, I. Arias, M. Arroyo, Phase-field modeling and simulation of fracture in brittle materials with strongly anisotropic surface energy, International Journal for Numerical Methods in Engineering 102 (3-4) (2015) 711–727.

[13] R. Mindlin, Micro-structure in linear elasticity, Archive for Rational Mechanics and Analysis 16 (1) (1964) 51–78.

[14] E. Aifantis, On the role of gradients in the localization of deformation and fracture, International Journal of Engineering Science 30 (10) (1992) 1279–1299.

[15] I. M. Gitman, H. Askes, E. Kuhl, E. C. Aifantis, Stress concentrations in fractured compact bone simulated with a special class of anisotropic gradient elasticity, International Journal of Solids and Structures 47 (9) (2010) 1099–1107.

[16] N. Auffray, R. Bouchet, Y. Brechet, Derivation of anisotropic matrix for bi-dimensional strain-gradient elasticity behavior, International Journal of Solids and Structures 46 (2) (2009) 440–454.

[17] V. Kouznetsova, M. Geers, W. Brekelmans, Multi-scale constitutive modelling of heterogeneous materials with a gradient-enhanced computational homogenization scheme, International Journal for Numerical Methods in Engineering 54 (8) (2002) 1235–1260.

[18] J. Dolbow, N. Moës, T. Belytschko, An extended finite element method for modeling crack growth with frictional contact, Computer Methods in Applied Mechanics and Engineering 190 (2001) 6825–6846.

[19] S. Dasgupta, D. Sengupta, A higher-order triangular plate bending element revisited, International Journal for Numerical Methods in Engineering 30 (3) (1990) 419–430.

[20] G. Zi, T. Belytschko, New crack-tip elements for xfem and applications to cohesive cracks, International Journal for Numerical Methods in Engineering 57 (15) (2003) 2221–2240.

[21] G. Sciarra, S. Vidoli, Asymptotic fracture modes in strain-gradient elasticity: size effects and characteristic lengths for isotropic materials, Journal of Elasticity 113 (1) (2013) 27–53.

[22] E. C. Aifantis, A note on gradient elasticity and nonsingular crack fields, Journal of the Mechanical Behaviour of Materials 20 (2011) 103–105.

[23] L. Vu-Quoc, V.-X. Tran, Singularity analysis and fracture energy-release rate for composites: Piecewise homogeneous-anisotropic materials, Computer methods in applied mechanics and engineering 195 (37) (2006) 5162–5197.

[24] Z. Yosibash, E. Priel, D. Leguillon, A failure criterion for brittle elastic materials under mixed-mode loading, International journal of fracture 141 (1-2) (2006) 291–312.

[25] R. de Borst, J. Remmers, A. Needleman, Mesh-independent numerical representations of cohesive-zone models., Engineering Fracture Mechanics 173 (2) (2006) 160–177.

Figures

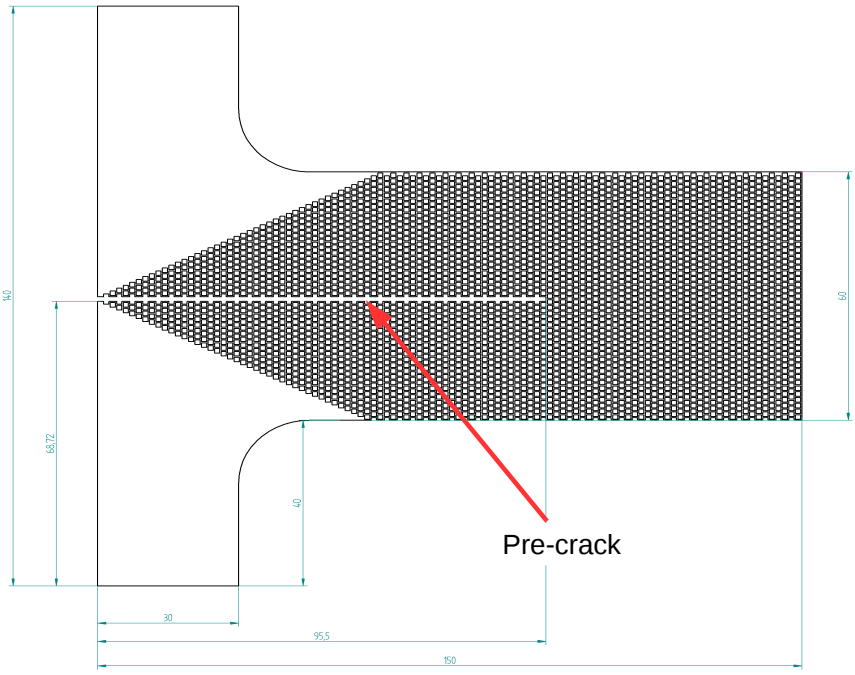

Figure 1: Specimen geomtry for the failure experiments.

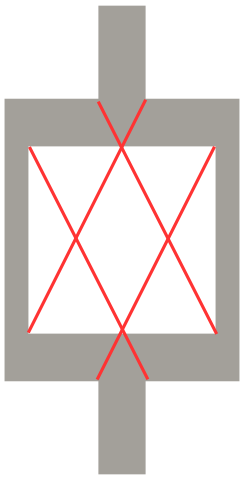

Figure 2: Admissible crack angles for the unit cell geometry.

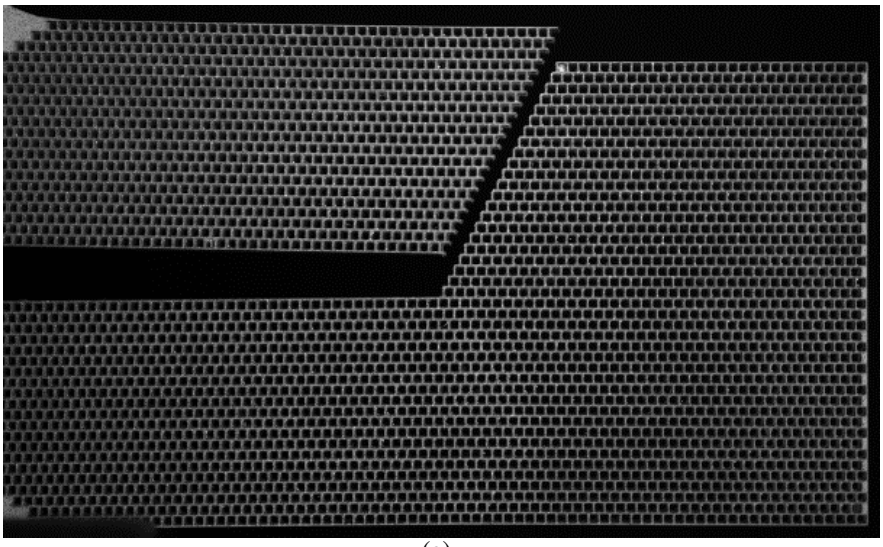

(a)

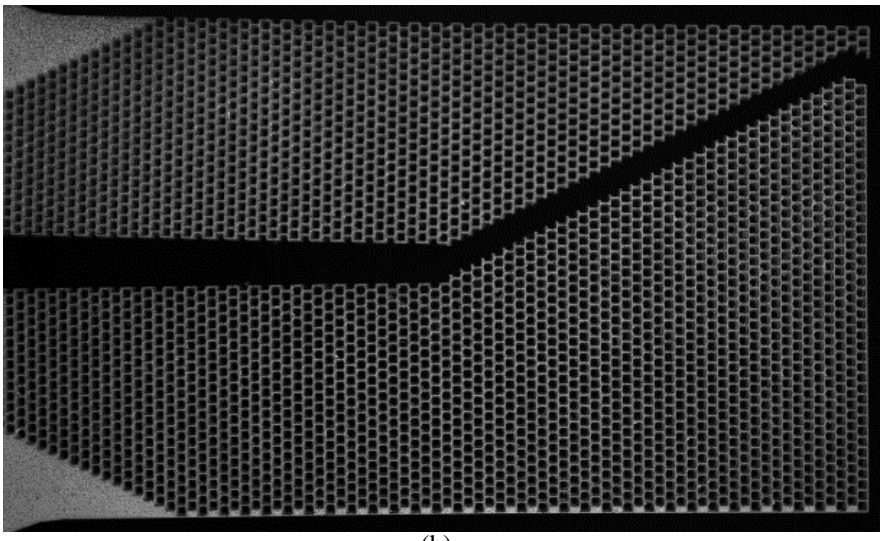

(b)

Figure 3: Experimental crack paths for two orientation of the material architecture: (a) 0°, (b) 90°.

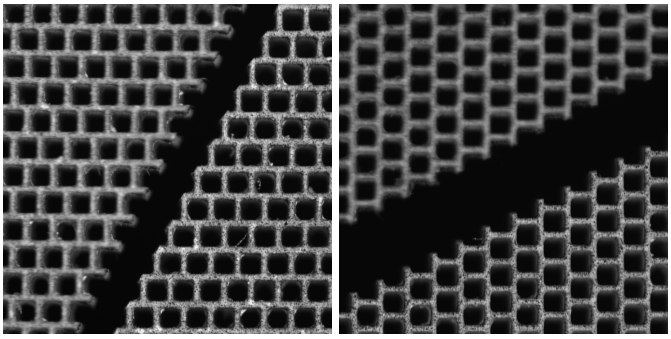

(a) (b)

Figure 4: Close view of the failure mechanisms in the analyzed architectured materials.

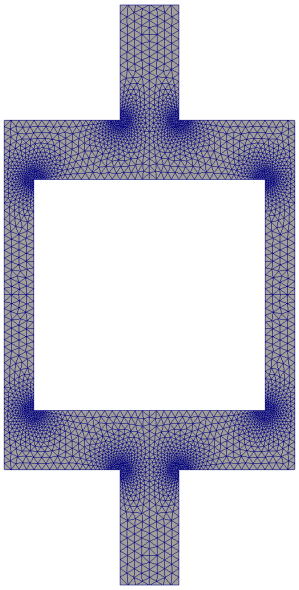

Figure 5: Mesh of the unit cell.

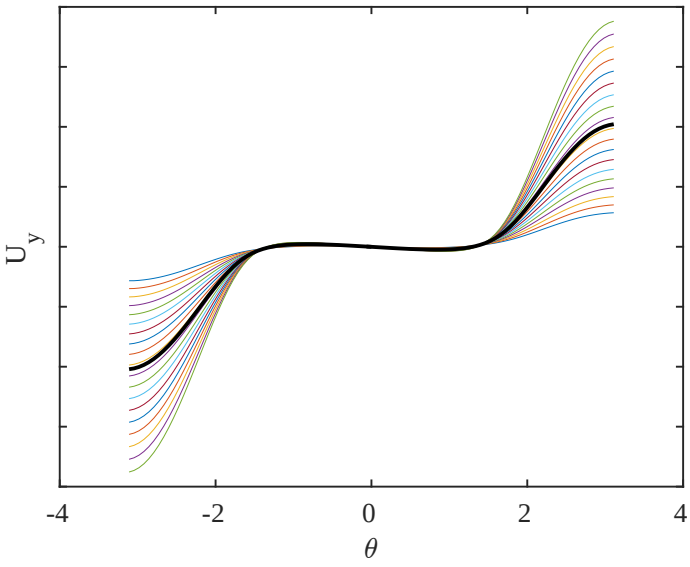

(a)

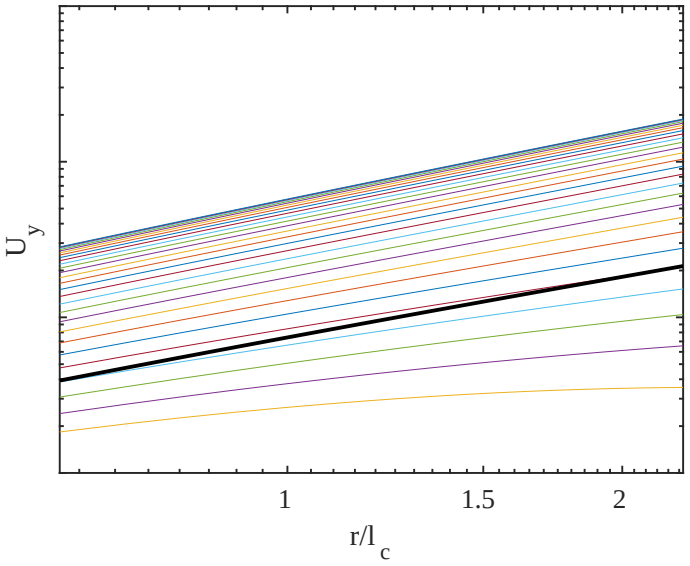

(b)

Figure 6: Illustration of the decomposition of the displacement around the crack tip as proposed in Equation (17). On the left, respectively right plot, the color lines correspond to the displacement field as function of θ, respectively r, for different values of r, respectively θ. The thick black line corresponds to g, respectively f.

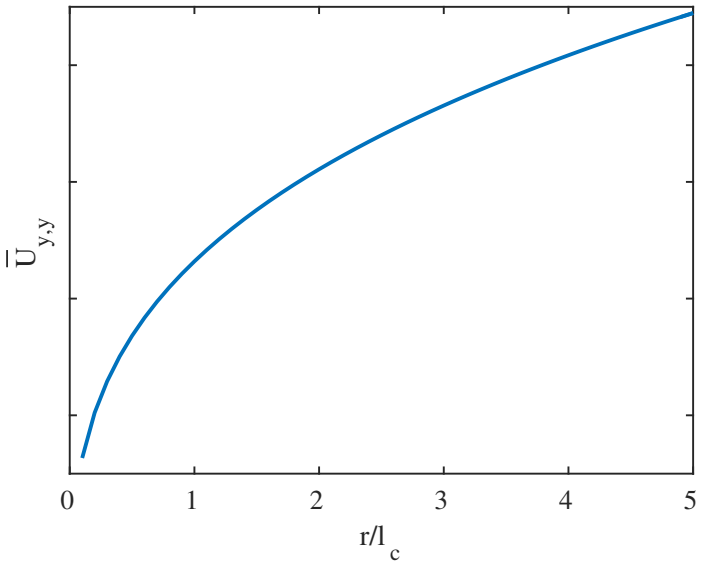

(a)

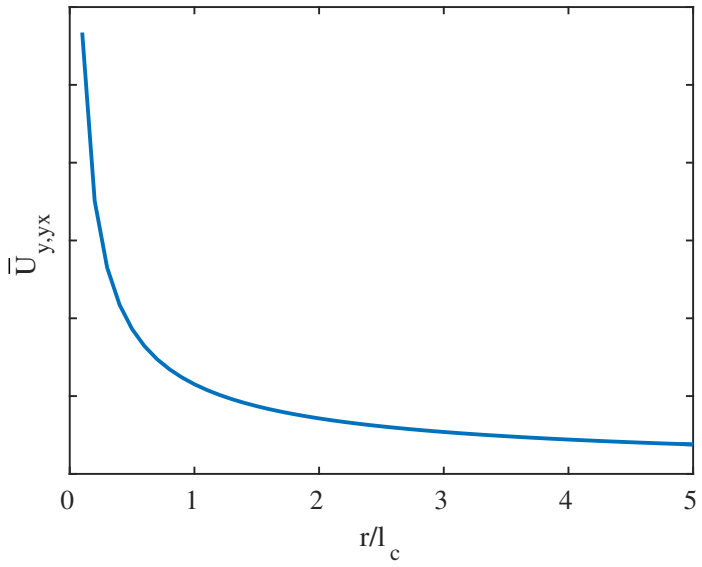

(b)

Figure 7: Variation of the average tip displacement derivative $\bar{U}_{y,y}$ and its gradient along the crack direction $\bar{U}_{y,yx}$ as functions of the averaging domain size r normalized by the unit cell size l_c.

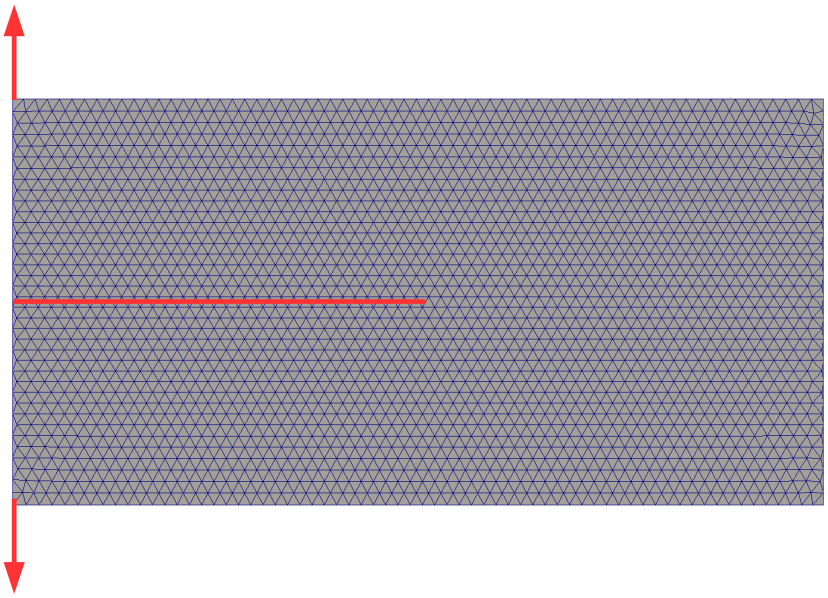

Figure 8: Mesh and boundary conditions of the sample for numerical simulations.

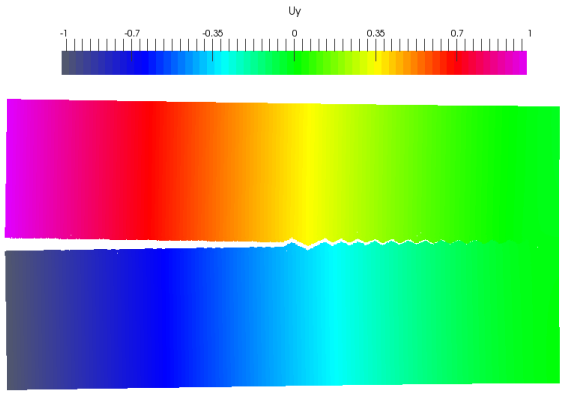

(a)

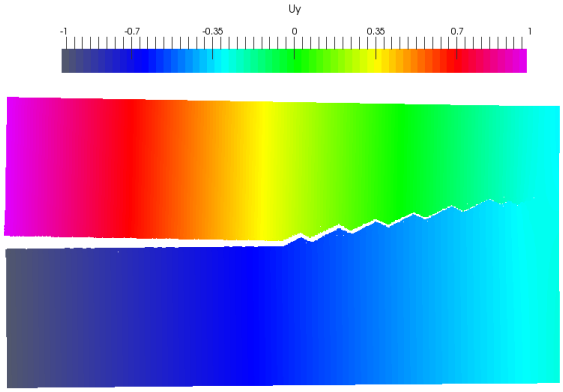

(b)

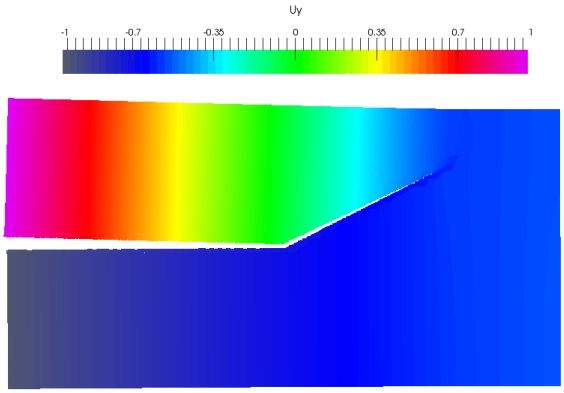

(c)

Figure 9: Normalized vertical displacement field at the end of crack propagation for the case: $D_2, \alpha = \pi/2$. Figures (a), (b) and (c) shows the results for $\frac{lc}{a} = 0.13$, $\frac{lc}{a} = 0.013$ and $\frac{lc}{a} = 0.0013$ respectively.

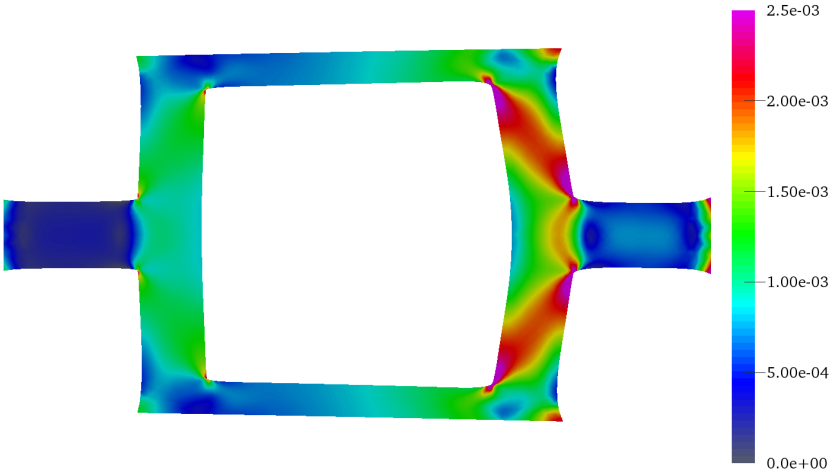

Figure 10: L_2 norm of the normalized strain field in the unit cell at crack initiation for the case $D_2, \alpha = \pi/2$.

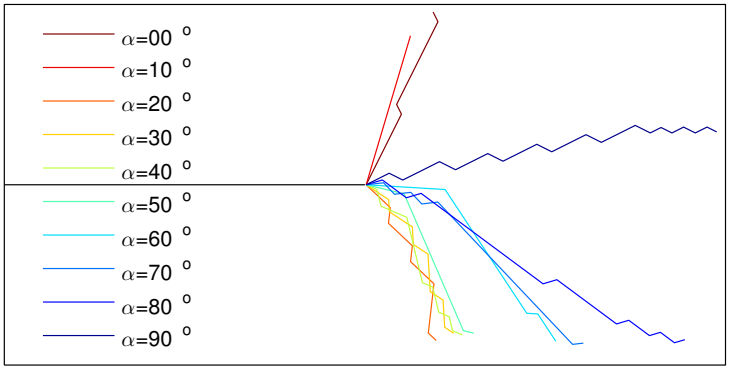

Figure 11: Comparison of the crack paths obtained for different orientation α of the unit cell for $\frac{l_c}{a} = 0.013$.

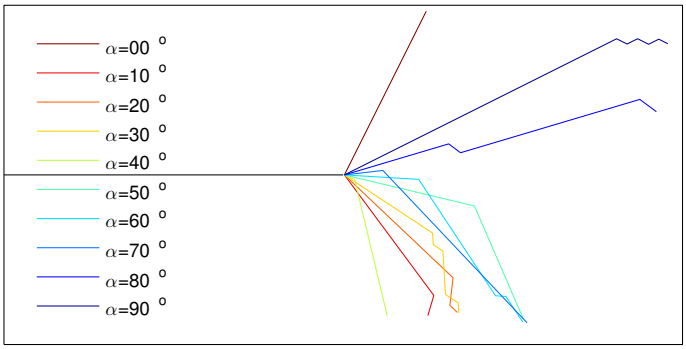

Figure 12: Comparison of the crack paths obtained for different orientation α of the unit cell with $\frac{lc}{a} = 0.0013$.

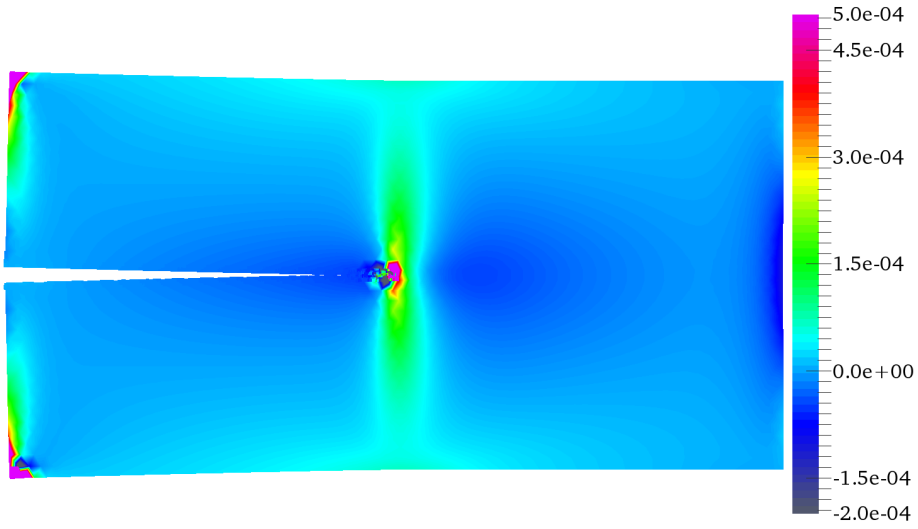

(a)

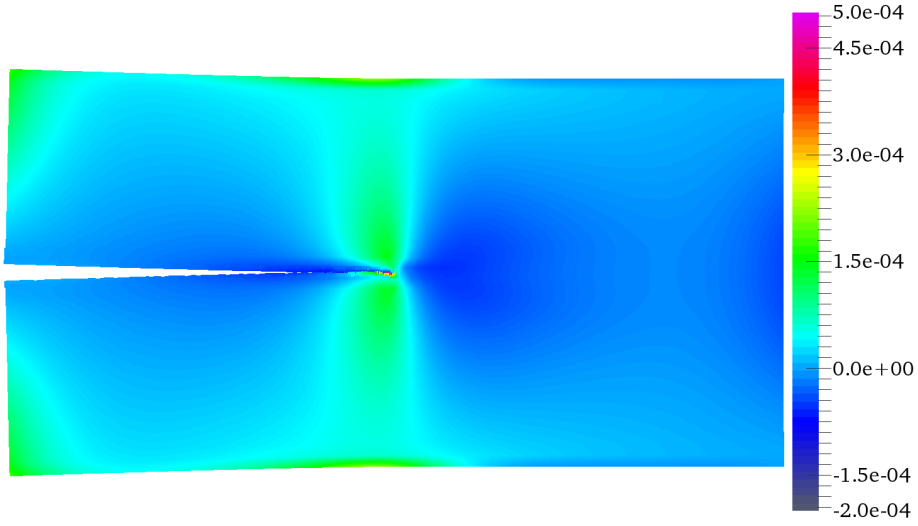

(b)

Figure 13: Comparison of the vertical component of the strain field E_{yy} for (a) $\frac{lc}{a} = 0.0013$ and (b) $\frac{lc}{a} = 0.13$.

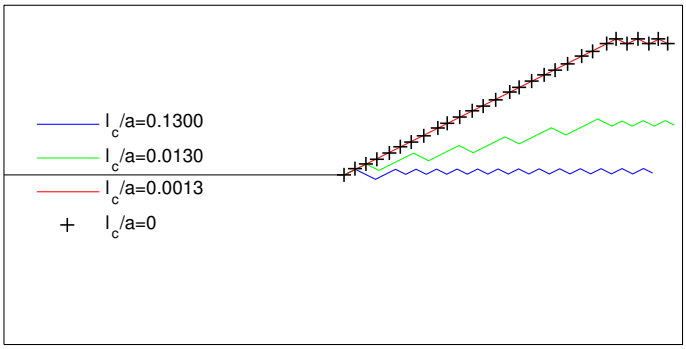

Figure 14: Comparison of the crack paths obtained with $\alpha = \pi/2$ and for different ratio between the unit cell size l_c and the crack length a. The results for the case when l_c goes to 0 (vanishing the second order term in the strain energy density) are also plotted with black crosses.

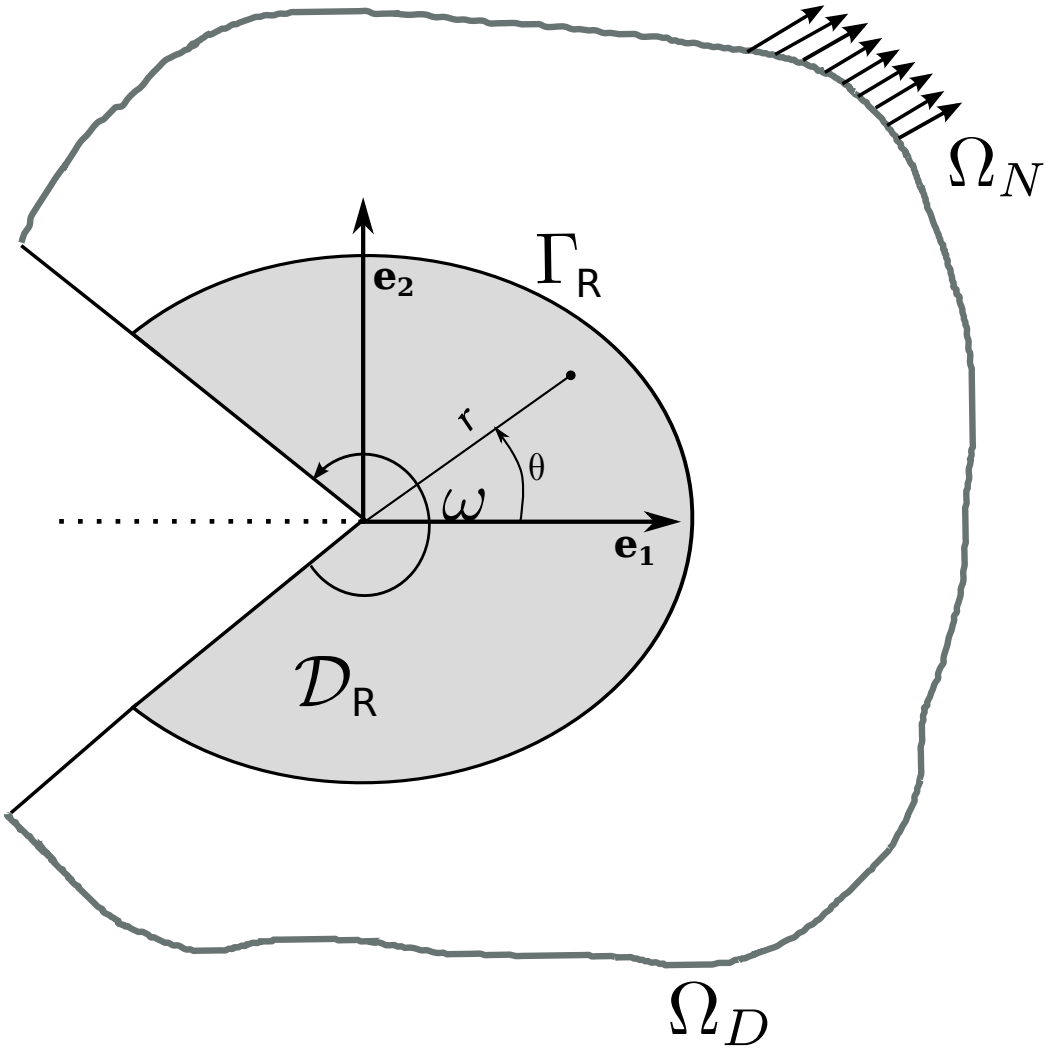

Figure 15: Definition of the domain around a notch for generalized stress intensity factors estimation.